CRYSTAL GROWTH & DESIGN

pubs.acs.org/crystal

Article

# Microstructure and Crystallographic Characteristics of Stenolaemate Bryozoans (Phylum Bryozoa and Class Stenolaemata)

Christian Grenier, Erika Griesshaber, Wolfgang W. Schmahl, and Antonio G. Checa*

Cite This: *Cryst. Growth Des.* 2023, 23, 965−979

Read Online

ACCESS | Metrics & More | Article Recommendations | Supporting Information



**ABSTRACT:** The bryozoan Cass Stenolaemata is currently represented by the Order Cyclostomata. They produce skeletons made exclusively of calcite crystals assembled into different microstructures. Despite extensive previous research, no appropriate crystallographic techniques have been applied to decipher their crystallographic organization. We present an in-depth crystallographic study of the microstructures of three extant species (*Fasciculipora ramosa*, *Hornera robusta*, and *Cinctipora elegans*) using scanning electron microscopy and associated techniques (energy-dispersive spectroscopy and electron backscatter diffraction), together with atomic force microscopy and micro-computed tomography. We differentiate two microstructures, foliated and tabular calcite, and establish consistent models of their crystallography. Foliated calcite of *F. ramosa* and *C. elegans* consists of co-oriented laths arranged with their *c*-axes parallel to their elongation axis and to their main surfaces, and one *a**-axis perpendicular to the latter (sheet texture). Tabular calcite of *H. robusta* consists of polygonal tablets with the *c*-axis as fiber axis (axial texture), perpendicular to the tablet surface. The foliated calcite of bryozoans is homeomorph to that of bivalves but has a significantly different crystallography. The tabular calcite of bryozoans lacks the spiral morphology of the tablet-shaped calcite of craniiformis brachiopods and has a different orientation of the *c*-axis with respect to the constituent tablets.

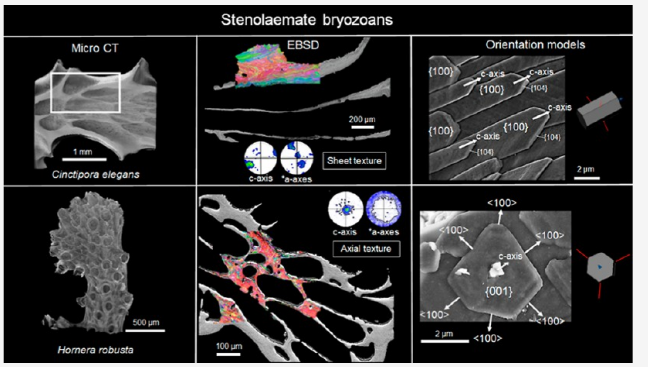


## 1. INTRODUCTION

The Phylum Bryozoa is the only one among invertebrates composed exclusively of aquatic colonial animals. They are found worldwide in both continental and marine waters, although the vast majority are found in the latter environment. Almost all marine bryozoans secrete calcium carbonate skeletons to build their colonies.[1] Together with their importance in the fossil record, they also register the effects of climate change in the marine environment and constitute a significant $CO_2$ fixation reservoir, along with many other marine calcifying proto- and metazoans (e.g., corals, mollusks, and foraminifera).[2] Currently, the estimated number of living bryozoan species is 6451 (WoRMS, accessed Oct 10, 2022),[3] distributed within three Classes. The Class Stenolaemata, which is the subject of this present study, contains 652 extant species, all of which inhabit marine environments and produce mineralized skeletons. They are currently represented by a single Order, Cyclostomata. Stenolaematans were the first bryozoans to appear, as early as in the Early Cambrian (Cambrian Age 3) and participated in the Cambrian radiation.[4] They spread their diversity during the Great Ordovician Biodiversity Event[5] and remained as the dominant group of bryozoans until the Upper-Jurassic radiation of the gymnolaematans.[6]

Bryozoans form colonies composed of clone individuals, called zooids. Depending on the species, each colony can be formed by a few to many thousands of zooids. Nevertheless, despite their identical genetic pool, zooids can have diverse morphologies (polymorphism) due to either a different developmental stage (ontogeny and astogeny) or because of functional differentiation depending on their role within the colony: feeding lophophorate zooids (autozooids), brooding zooids (gonozooids), defensive zooids (avicularia), and structural zooids (kenozooids).[1] This phenotypic plasticity has played a fundamental role in the evolutionary and adaptive success of this phylum throughout its history.[7]

Bryozoans build their skeletons of calcium carbonate. They first form a thin organic periostracum, mainly composed of chitin and mucopolysaccharides, secreted by a stratum of palisade cells.[8] Then, the periostracum becomes the seeding sheet for the calcium carbonate layers, which are secreted by

**Received:** October 11, 2022
**Revised:** December 29, 2022
**Published:** January 9, 2023

epithelial cells immediately adjacent to the palisade cells. Calcite has been described as the only mineral component of the Stenolaemata skeleton, unlike bryozoans from the class Gymnolaemata, where we can find either calcite, aragonite, or both within the zooids of a single species.[8]

Based on scanning electron microscopy (SEM) imaging, previous studies described different types of microstructures in recent and fossil stenolaemate bryozoans. Söderqvist[9] was the first to image the microstructure of cyclostome bryozoans with SEM and noted the presence of two calcite layers: a thin outer prismatic layer and a thicker inner lamellar layer. Boardman and Cheetham[10] used thin sections and SEM imaging to describe the colony structure, the zooid arrangement, and the skeletal fabric (laminated lath-like fibers) in "tubular" (i.e., stenolaemate) bryozoans. Tavener-Smith and Williams[8] described the walls of cyclostome zooids as being composed of a thin outer layer of granular calcite and an inner layer with a laminated structure. Brood,[11] in trying to use the skeletal microstructure as a new character in phylogeny, reported three different layers in the walls of the order Cyclostomatida: an inner (granular), a middle, and an outer layer (both laminar). "Semi-nacre calcite" was first used to name the rhombic and hexagonal platelets in bryozoans[12] and grouped several previously described microstructures in both Cheilostomata and Cyclostomata classes. It is worth noting that the calcitic semi-nacre was previously described in craniid brachiopods[13,14] as "calcitic laminae that grow spirally from single or double screw dislocations". Simonet Roda et al.[15] disregarded the term "semi-nacre" because of their lack of affinity with nacre and considered this microstructure as being formed by tablet-shaped calcitic elements. Following these authors, we will adopt the term tabular calcite for the "semi-nacre" of bryozoans from here on.

Boardman et al.[16] described the shell ultrastructure of their new stenolaemate family Cinctiporidae, demonstrating the presence of an inner layer of transverse fibrous crystallites covered by a laminated layer made of lath-like crystals. Later, Taylor and Jones[17] described the microstructure of *Hornera robusta* as made up of polygonal tablets. In a review of the skeletal ultrastructure of the Cyclostomata, Taylor and Weedon[18] summarized a total of six fundamental ultrastructural fabrics based on SEM images of 87 different species: granular, planar spherulitic, transverse fibrous, foliated, rhombic semi-nacreous, and hexagonal semi-nacreous (their terminology) (Figure S1).

Although previous studies described bryozoan microstructures in detail based on SEM images, very few have provided crystallographic data of the prevailing crystal orientations. Based on the SEM images, Taylor and Weedon[18] suggested that the laths of the foliated fabric had a main external surface of the {104} type ($\{10\bar{1}1\}$ in their notation), and the *c*-axis was inclined by 45° in the direction of elongation (growth) of the laths. The elongation proceeded by accretion of the {104} faces looking in that direction. They differentiated a second variety, their transverse microstructure, which was made by laths growing along a direction perpendicular to that of the foliated microstructure. In their "rhombic semi-nacre" (tabular microstructure), the tablets also had the same distribution of crystallographic axes, but they grew at their periphery in all directions. Conversely, they explained the hexagonal variety of semi-nacre as platy crystals growing at their periphery, where the *c*-axis is perpendicular to the top surface, which would then be a {001} surface, with oblique {104} lateral faces. Studies on the crystallography of the "laminated calcite" (tabular calcite) of the cyclostome bryozoans *Hornera currieae* and *H. robusta* with electron backscatter diffraction (EBSD)[19,20] concluded (in line with Taylor and Weedon)[18] that the *c*-axes were oriented perpendicular to the skeletal walls, whereas the *a*-axes were randomly oriented "laying predominantly in the plane of the wall". Contrary to other groups of biomineralizers such as corals, mollusks, and brachiopods, where numerous and complete crystallographic studies of their microstructures have been carried out,[15,21−23] there is still much to learn about in bryozoans. Accordingly, we decided to conduct a thorough study of the distribution and crystallography of the microstructures of the two main groups of bryozoans, cheilostomes and cyclostomes. In this study, we provide new crystallographic data for three cyclostome species: *Fasciculipora ramosa*, *H. robusta*, and *Cinctipora elegans*. We studied their microstructures using SEM imaging, energy-dispersive spectroscopy (EDS), and EBSD. Additional data were obtained with atomic force microscopy (AFM) and micro-computed tomography (micro-CT). We provide specific modes of crystal orientations for the microstructures distinguished in the mentioned stenolaemate species, in particular the foliated and tabular calcite, and compare their similarities and differences with homeomorphic microstructures of other phyla.

## 2. MATERIALS AND METHODS

**2.1. Materials.** We analyzed three different species of Stenolaemata, Order Cyclostomatida: *F. ramosa* (d'Orbigny, 1842), *H. robusta* (MacGillivray, 1883), and *C. elegans* (Hutton, 1873). Fragments of colonies were obtained from the palaeontological and zoological reference collections of the Natural History Museum (London). Provenance and collection data are summarized in Figure S2.

**2.2. Micro CT.** Fragment of colonies from both *C. elegans* and *H. robusta* were selected for micro-CT analyses. The fragments were fixed to the tip of a needle holder with glue. The measurements were performed in an X-ray microtomograph Xradia 510 VERSA ZEISS (CIC, UGR), with a resolution of 0.7 $\mu$m at 60 kV and 4 W, using the 4× magnification objective. The selected imaging mode selected was "bin 1" of the detector. The exposure time was 30 s per projection with a LE1 filter and a pixel size of 0.9951 $\mu$m. The total number of projections was 3201. Micro-CT images were processed with Dragonfly software to obtain three-dimensional images and videos of both the structure of the colony as well as the inner volume occupied by the zooids and the funicular system.

**2.3. Scanning Electron Microscopy.** Fragments were cleaned by immersion in commercial bleach (~5% active chlorine) for 10 min in a stirring set. Then, the bleach solution was removed by several sonication washings in Milli-Q water for 2−3 min each. Once oven-dried at 40 °C for 2 h, some fragments were directly selected for observation, whereas others were embedded in epoxy resin (EpoFix, Struers). After 48 h of hardening, the surface of interest was ground in successive steps (with electroplated diamond discs: 360, 600, 1200, and 3000 ANSI/CAMI US grit number) and then polished with high-density wool felt pads (adding first 1 $\mu$m and then 1/4 $\mu$m of polycrystalline diamond suspension, Struers), until reaching a mirror polishing surface (Hi-Tech Diamond polishing machine, All-U-Need model). Some samples, both polished and unpolished, were immersed in an etching and decalcifying solution (2.5% glutaraldehyde, 0.25 M HEPES buffer, and 0.05 M EDTA) for 2−5 min in an orbital shaker. SEM observations were performed after carbon coating (Emitech K975X carbon evaporator) using secondary electron (SE) and backscatter electron detectors in a field emission SEM FEI QemScan 650 F (Centro de Instrumentación Científica, CIC, University of Granada, UGR).


https://doi.org/10.1021/acs.cgd.2c01149
Cryst. Growth Des. 2023, 23, 965−979

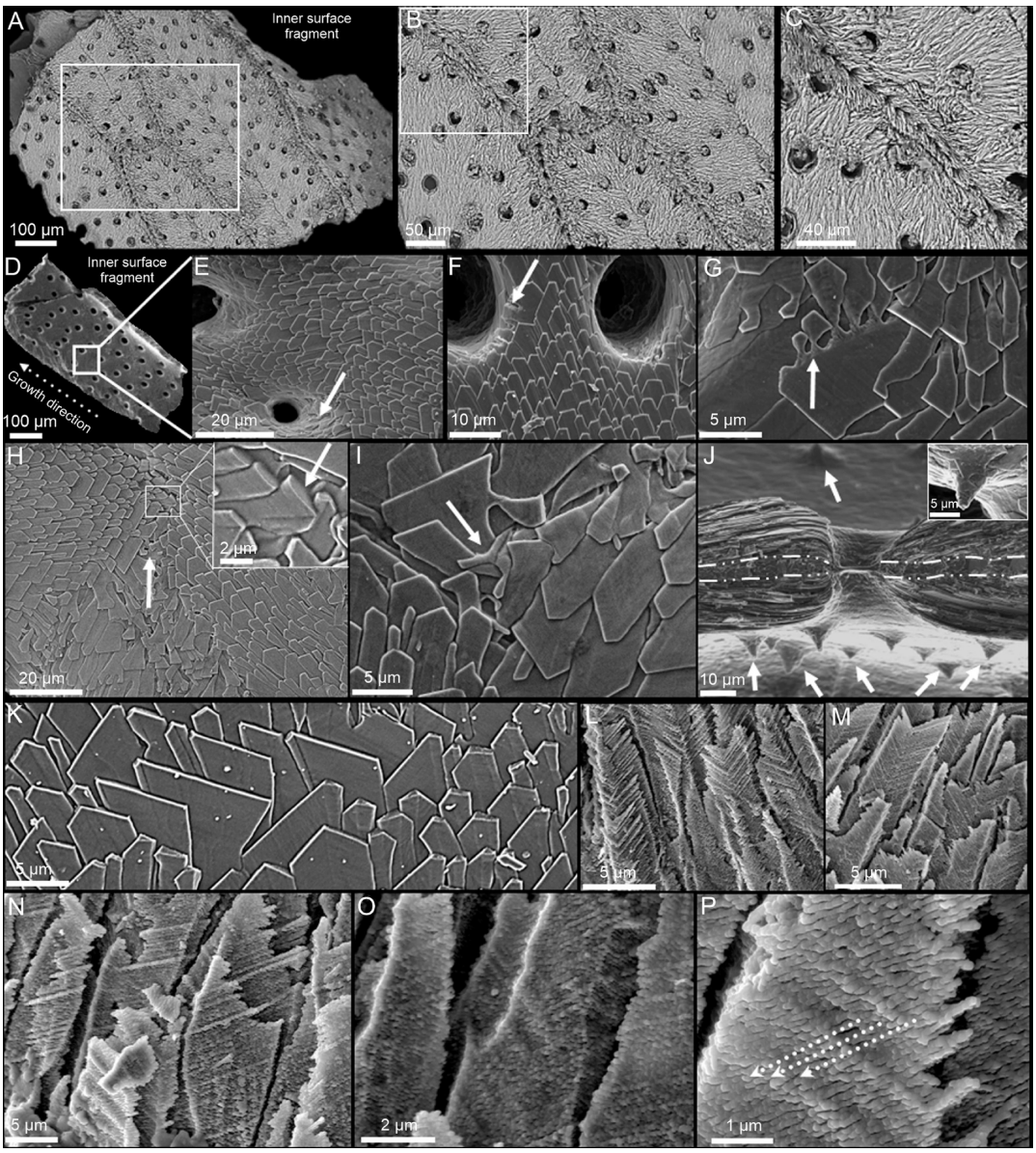


**Figure 1.** Foliated calcite of *F. ramosa*. (A–C) Views, at increasing magnifications, of the inner surface of a few zooid chambers from unpolished and slightly decalcified colony fragments. (D–K) Unpolished bleached surfaces. (D) Representative fragment of a zooidal chamber. (E–K) Foliated calcite of the inner surface of the chamber. Note the ordered arrangement of the calcite laths, with their characteristic arrowhead endings. Arrows in (E–I) point to regions where laths adapt to changes in the surface topography by bending and/or bifurcating. The inset in H shows the highly inclined smooth surfaces of the lath endings (arrow). (J) Cross section of an interzooidal wall showing a central granular layer (delimited by white dashed lines). Laths are parallel to the inner surfaces of both chambers. The wall is interrupted by a mural pore that connects two adjacent zooids. Mural spines are widely distributed over the inner surfaces (arrows). The inset shows a mural spine. (L–P) Slightly etched surfaces with highly marked growth lines. (N–P) Close-up views of the laths displaying a patent surface nanoroughness. Nanoprotrusions arrange in particular directions (dashed lines in P).

**2.4. Atomic Force Microscopy.** Two colony fragments of *F. ramosa* and *H. robusta* were cleaned by immersion in commercial bleach (~5%, 1 h) and subsequently reduced to small fragments oriented so that the inner chamber surfaces were exposed. For imaging, an AFM Park Systems NX20 equipped with a cantilever MikroMasch ACTA ($K$ = 40 N/m, $F$ = 320 kHz) (CIC, UGR) was used in Tapping and PinPoint modes to record height, amplitude, and phase signals. Images were obtained with a Smart Scan v12 and processed using XEI software (4.3.0. Build2, Park Systems).

**2.5. Electron Backscatter Diffraction.** Shell samples were embedded in epoxy resin, sectioned, and subjected to several sequential mechanical grinding and polishing steps. The last two polishing steps consisted of etch-polishing with colloidal alumina in a vibratory polisher. For EBSD analysis, the samples were coated with 4–6 nm of carbon (Leica EM ACE200). Measurements were taken on a Hitachi SU5000 field emission SEM, equipped with an Oxford Instruments NordlysNano II EBSD detector. The SEM was operated at 20 kV, and Kikuchi patterns were indexed with the CHANNEL 5 HKL software. EBSD measurements were performed in step increments between 200 and 500 nm.

Information obtained from EBSD diffraction measurements is presented as band contrast measurement images and as inverse pole figure (IPF) maps. White or dark regions in the band contrast maps correspond to a higher or weaker signal strength, respectively, of the EBSD-Kikuchi diffraction patterns. The IPF maps are color-coded crystal orientation images, where similar colors indicate similar orientations. The term texture relates to the orientation of the crystallographic axes within a material. The texture is represented by


https://doi.org/10.1021/acs.cgd.2c01149
Cryst. Growth Des. 2023, 23, 965–979

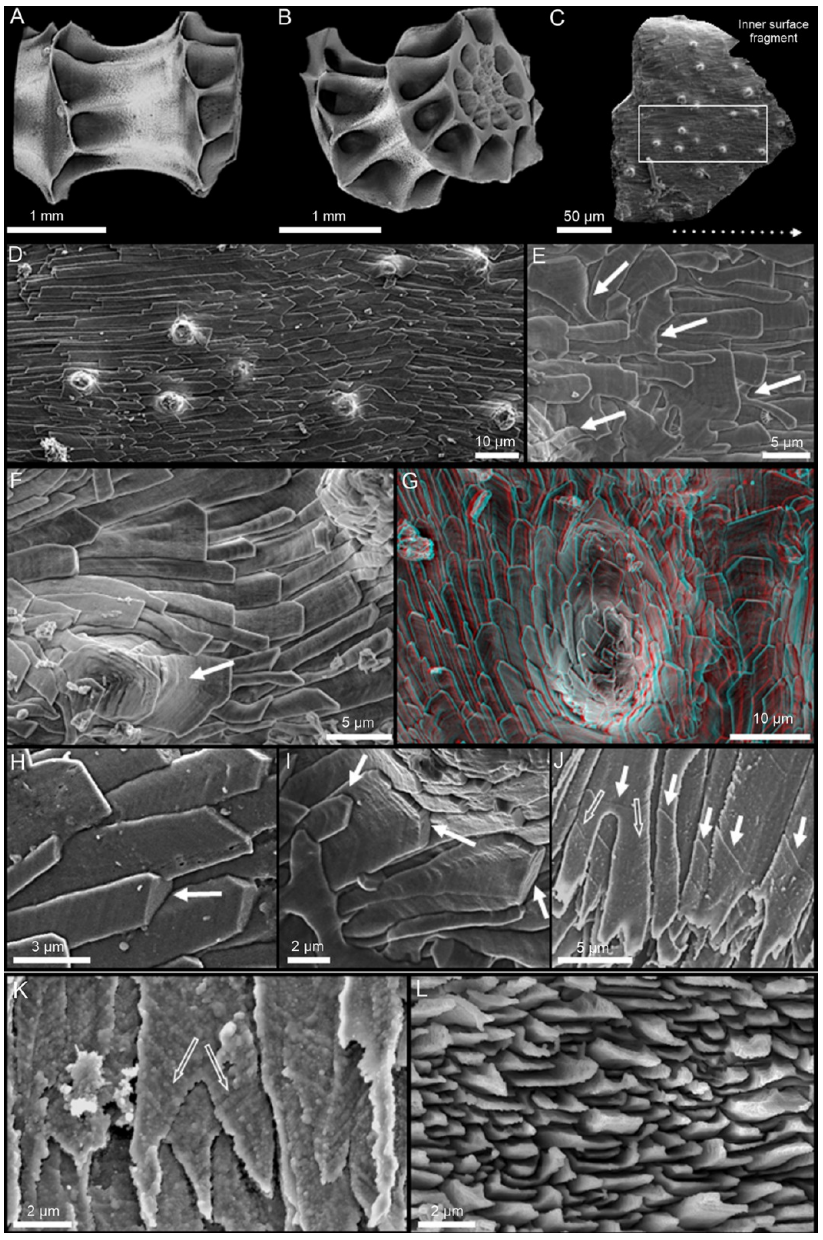


**Figure 2.** Foliated calcite from unpolished surfaces of *C. elegans*. (A,B) Lateral and oblique views (micro-CT images) of the cylindrical colony fragment analyzed (see also Figure S3). (C−I) Unpolished bleached inner surfaces. (C) Representative fragment of a zooidal chamber. The growth direction is indicated by the bottom dotted arrow. (D−I) Detailed views of the foliated calcite. (D) Close-up of the area framed in (C) showing preferential alignment of the laths. (E,F) Calcite laths exhibit a high growth plasticity (arrows) by tightly adapting to the surface protuberances. (G) Is an anaglyph of a surface protuberance (to appreciate the 3D effect, red-cyan glasses have to be used). (H,I) The terminal and highly inclined surfaces of the laths are smooth (arrows). (J,K) Slightly etched surfaces. Some growth lines are highly marked and can be correlated across different laths (solid arrows), even between laths resulting from splitting of a parental lath (empty arrows). The surface nanoroughness is clearly exposed in (K). (L) Cross-sectional view of the laths, revealing their space-filling arrangement.

stereographic projections in the same spatial orientation as the corresponding EBSD map, known as PFs. The PFs are presented either as individual data points or, in the contoured version, as the strength of the clustering of poles. When we show the contoured data, we use the lowest possible degree for half-width (5°) and cluster size (3°). The half-width controls the extent of the spread of the poles over the surface of the project sphere. A cluster comprises data with the same orientation. We also provide the multiple of uniform distribution (MUD) values. A high MUD value indicates high crystal co-orientation, while low MUD values point to random orientation or low crystal co-orientation. Very high values (MUD > 700) indicate single crystallinity of the crystal.

## 3. RESULTS

**3.1. Micro-CT Reconstruction.** The studied colony fragment of *C. elegans* (Figure S3) has a cylindrical erect morphology. Two levels of concentrically disposed zooids can be observed (Figure S3A). In the inner central region, we can see smaller, disordered chambers of different sizes that may correspond to enclosed dormant autozooids (kenozooids) (Figure S3A). In the longitudinal section (Figure S3B), the autozooids have a conical tubular shape, which is significantly wider at the aperture. The zooids are connected to each other through interzooidal pores, which are more abundant toward


https://doi.org/10.1021/acs.cgd.2c01149
Cryst. Growth Des. 2023, 23, 965−979

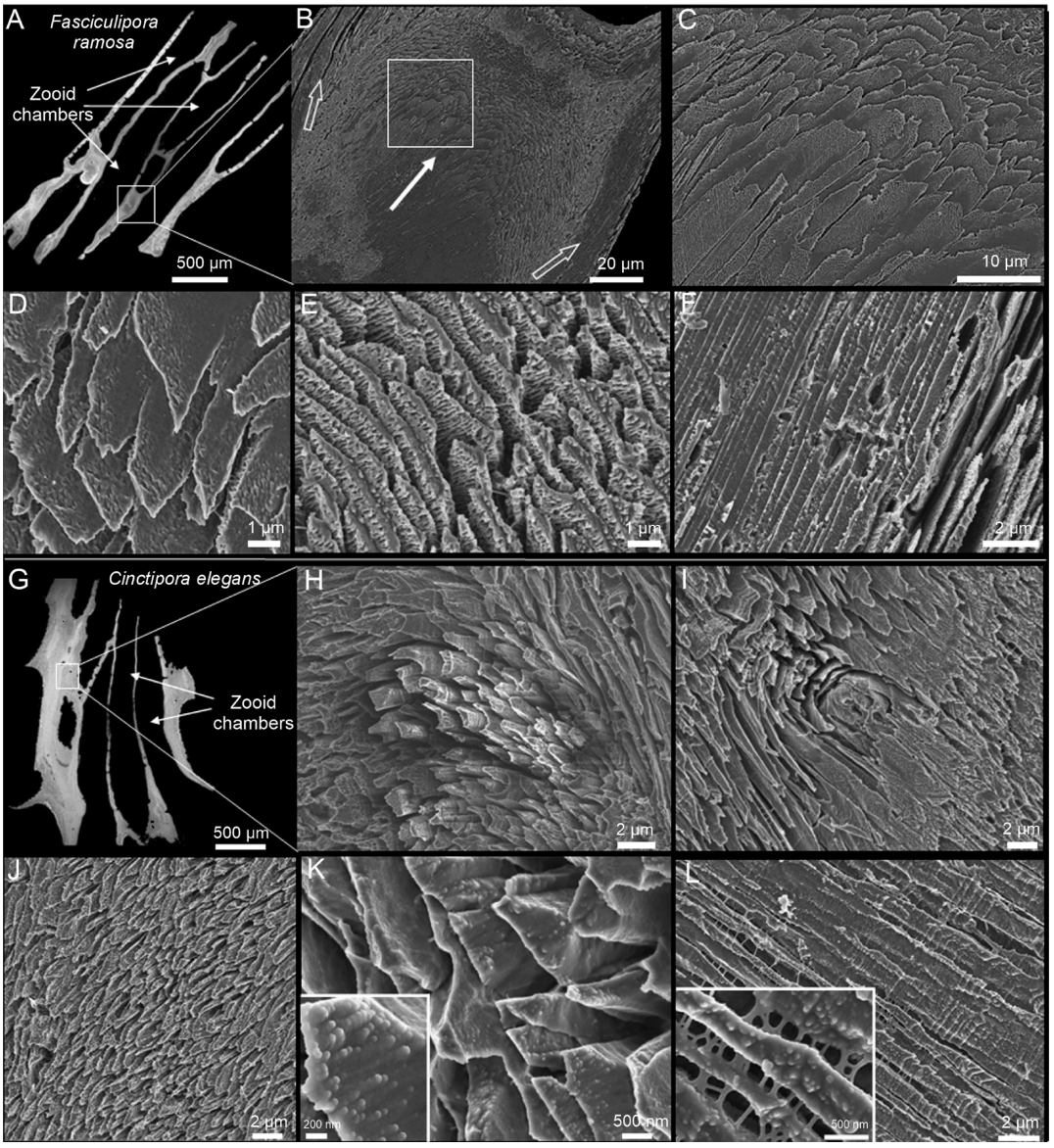


**Figure 3.** Polished and slightly decalcified colony fragments of *F. ramosa* (A–F) and *C. elegans* (G–L). (A,G) General views of the colonies. (B) Detail of a sectioned chamber. Laths exhibit different morphologies depending on how they have been sectioned: parallel to their main surfaces in the center of the chamber (solid arrow) and perpendicular to it toward the sides (empty arrows). (C,D) Details of the central area (framed in B). (E,F) Details of the margins of the chamber. Laths have been sectioned transversal (E) and parallel (F) to their growth axes. (H,I) Sections of two protuberances, showing the disposition of the calcite laths inside and around them. (J,K) Laths sectioned transversal to the growth axis. Their space-filling behavior is evident. The surface nanoroughness is neat in (K) (inset). (L) Laths sectioned parallel to the growth axis. Organic threads extend between them (inset).

their central region. The interzooidal walls, which separate two generations of autozooids, are interconnected by special pores called hypostegal pores (white arrows, Figure S3B). 3D reconstruction reveals the inner volumes of the zooids, the hypostegal pores, and the funicular system (white arrows) (Figure S3C).

The zooids of *H. robusta* build branched erect colonies, arranged in a fan-like manner. The free-walled zooids present long tubular chambers, slightly widening toward the aperture (Figure S4). The branch has an abfrontal (posterior) part from which the lateral autozooids bud and grow (Figure S4A). Autozooids curve toward their frontal part. The boundaries between adjacent zooids and the skeleton (shown with cyan and gold colors in Figure S4B) can be distinguished. The communicative channels (funicular system, shown in Figure S4C) connect two adjacent zooids along the entire length of the chamber. New generations of autozooids grow through parental budding (dashed circles, Figure S4C). They are separated by the interzooidal walls but are, however, connected through the hypostegal pores (white arrows, Figure S4C).

**3.2. SEM Imaging.** In the three investigated bryozoan species, we identified two calcite microstructures: foliated and tabular. Foliated calcite was found in *F. ramosa* (Figure 1) and *C. elegans* (Figure 2), and formed, for both species, the skeleton of the entire colony. From the SEM images of unpolished fragments (Figures 1 and 2), we can observe that the calcite laths are co-oriented and, in general, elongate in the growth direction of the zooidal chambers. The main planar crystal faces are parallel to the chamber surface. The laths show some degree of imbrication, and their exposed part ranges in


https://doi.org/10.1021/acs.cgd.2c01149
Cryst. Growth Des. 2023, 23, 965–979

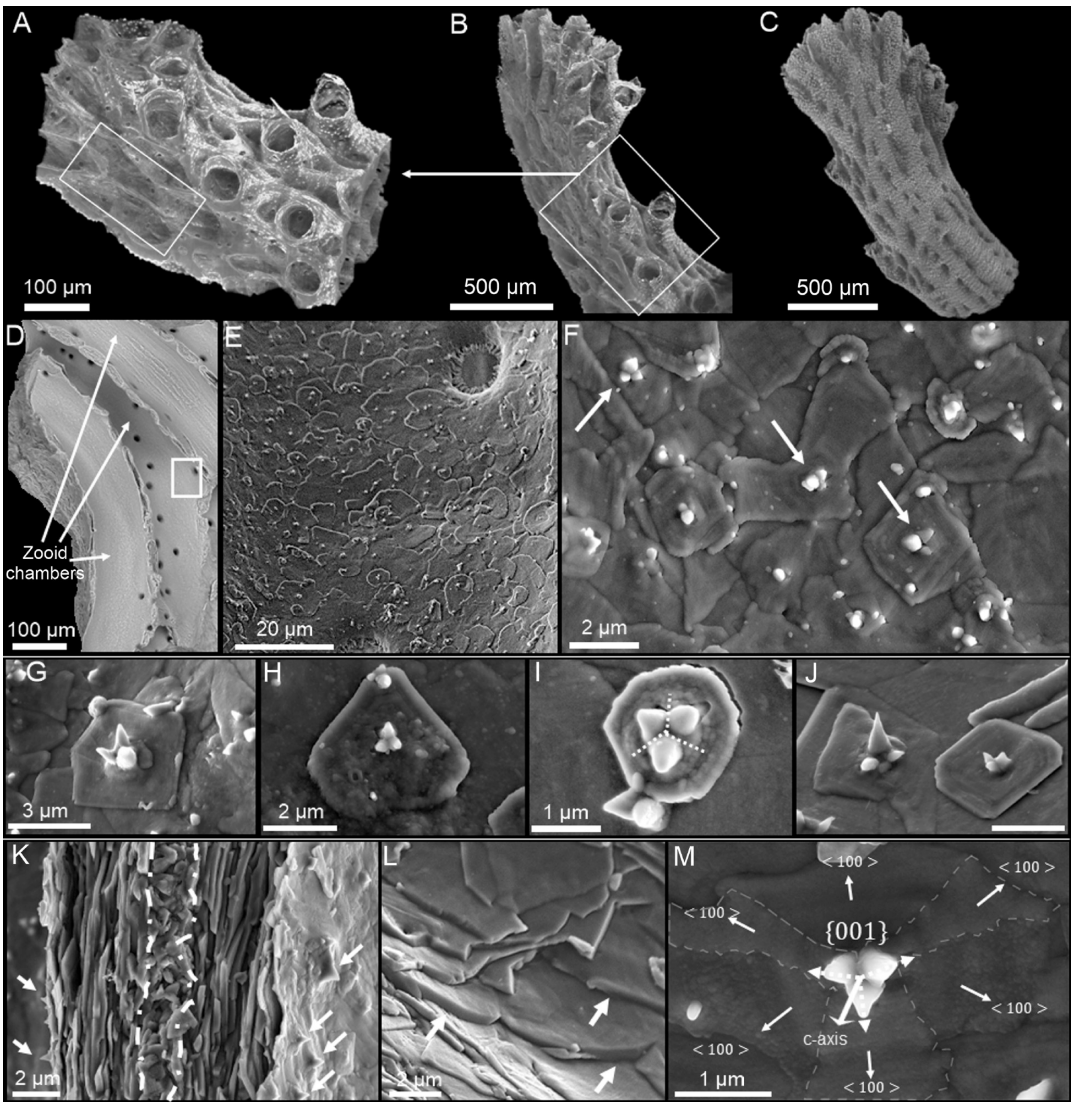


**Figure 4.** Tabular calcite of the interior of a colony fragment of *H. robusta*. (A–C) Oblique (partly sectioned) (A,B) and posterior (C) views (micro CT images) of the colony fragment analyzed (see also Figure S4). (D) Fractured fragment showing the characteristic tubular shape of the zooids, which are connected by interzooidal pores. (E) Inner surface of a zooidal chamber covered by polygonal tablets. (F) Close-up view of the inner surface. The white dots correspond to triple-spiked structures at the centers of the tablets (arrows). (G–J) Close-up views of polygonal calcite tablets. Growth lines and nanoroughness on the surfaces of the tablets are clearly discernible. The triple-spiked outgrowths measure from 100 to 300 nm in height, exceptionally up to 1 $\mu$m (J). (K) Cross section of an inner wall separating two zooid chambers. A central granular layer (marked by dashed lines) can be appreciated. The tablets are parallel to both surfaces and the spikes point perpendicularly (arrows). (L) Fracture showing the smooth lateral surfaces of the tablets (white arrows). (M) Single tablet with central triple spike. Crystallographic faces have been tentatively indexed. The spikes diverge at equal angles (they appear distorted in the present view due to the tablet being slightly inclined with respect to the plane of the image).

length from a few to several tens of microns. Their width ranges from 1 to 10 microns, being longer and thinner in *C. elegans*. The characteristic arrowhead ending of the laths can be acute or obtuse, sometimes truncated by a transversal surface (Figures 1D–K and 2D–I). Although laths tend to show a predominant growth direction, it is not uncommon that they change their orientation by bending, sometimes accompanied by bifurcation (white arrows, Figures 1E–I and 2E,F). This feature allows them to adapt to changes in the topography, such as protuberances, pores, transversal walls, depressions (Figures 1F,I,J and 2F,G), and internal mural spines (inset in Figure 1J). At higher magnification, the growth lines are visible on the main planar surfaces of the laths (Figures 1I,K and 2E,F,G_I), becoming clearly discernible after decalcification (*Fasciculipora ramosa*, Figure 1L–P; *C. elegans*, Figure 2J;K). This same treatment reveals the rough nanostructure of the laths (Figures 1O,P and 2K).

On polished colony fragments of *F. ramosa* and *C. elegans* (Figure 3A,G, respectively), the aspect of calcite laths differs depending on whether they are sectioned parallel (e.g., solid arrow in Figure 3B) or transversal (empty arrows in Figure 3B) to their main upper surfaces. The laths demonstrate their whole width in sections parallel to their main surfaces (i.e., to the zooid surfaces) (Figure 3C,D), whereas they have rectangular, narrow shapes when cut transversely (Figure 3E,F). In cross sections, their space filling disposition can be appreciated, even within the interior of protuberances (Figures 2L and 3H–K). Upon decalcification, the presence of very thin


https://doi.org/10.1021/acs.cgd.2c01149
Cryst. Growth Des. 2023, 23, 965–979

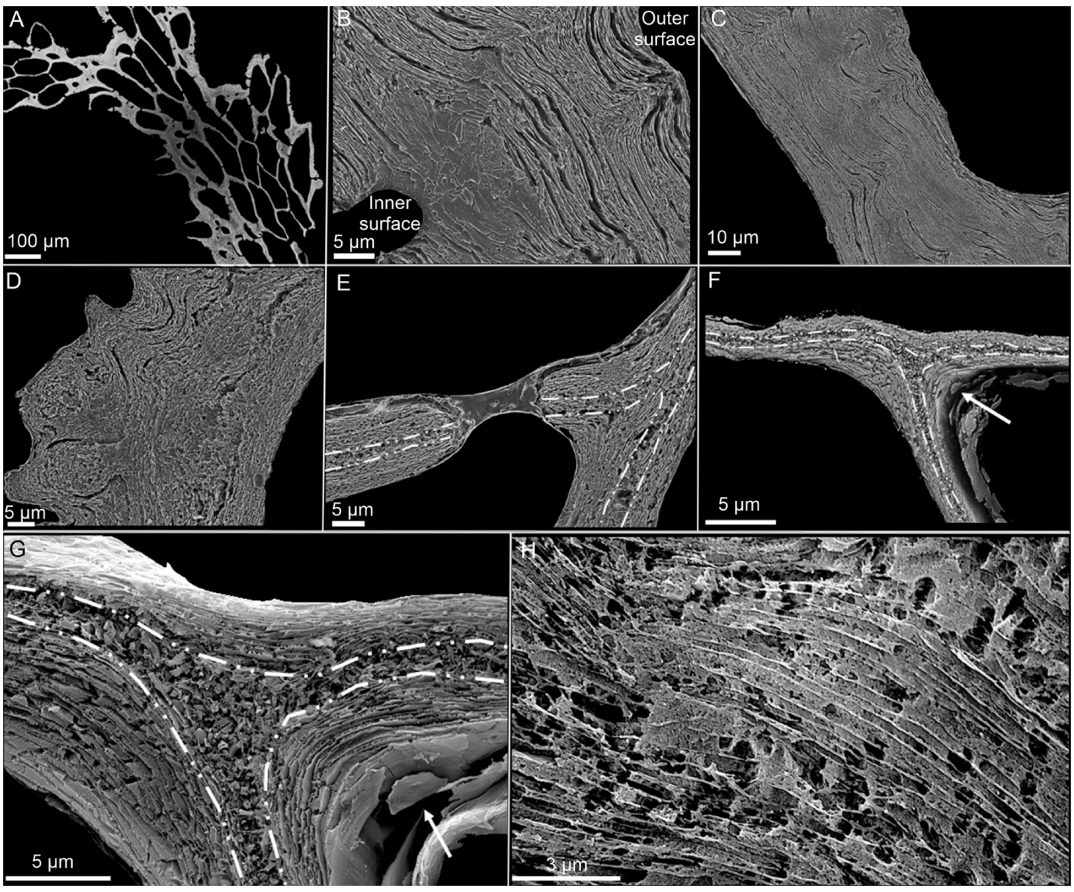


**Figure 5.** Morphology and microstructure of *H. robusta* (A). Polished and partly decalcified colony. (B−D) External wall section showing the multi-layered undulated patterning that flattens progressively toward the inner surface. The peaks correspond to the external protuberances. (E−G) Cross section of an inner wall. The sections are entirely composed of tabular calcite (arrow in F), except for the central granular layer (marked with dashed lines). (H) Details showing the organic membranes running uninterruptedly between the lamellae of polygonal tablets.

intervening organic threads is revealed (i.e., in *C. elegans*, Figure 3L).

Tabular calcite, formerly described as semi-nacre,[12] is only present in *H. robusta* (Figures 4, 5, S5, and S6) and constitutes the bulk of the skeleton of the entire colony (Figures 4A−C). Calcite tablets completely carpet the inner surface of the zooidal chambers (Figure 4D,E). They have polygonal morphologies and are arranged parallel to the surface, stacked onto each other, and unevenly distributed (Figure 4E,F). Their number of sides ranges from three to six. The range of tablet diameters is between 3 and 10 $\mu$m, and their average thickness is ∼150 nm (Figures 4G−J, S5, and S7). The edges of the tablets may be straight or irregular. Adjacent tablets tend to overlap, except when their edges are at the same height (white arrows in Figure S5B,C,E,F). Under high magnification, the main surfaces of the polygonal tablets reveal a rough nanostructure (Figure 4G−I), similar to the surface of the laths that form the foliated calcite. Concentric growth lines, mainly parallel to the edges of the tablets, are also observable on their main surfaces (Figures 4F,H−J,M and S5B,D−N). In the cross section of the inner walls that separate adjacent zooidal chambers (Figure 4K), we can discern a thin central layer made of irregular, sometimes polyhedral, calcite grains (delimited by a dashed line in Figure 4K). Immediately adjacent, in both growth directions, the tabular layer becomes organized, and the tablets align parallel to the central granular layer, which is arranged in laminae. As previously described,[17] virtually all the tablets in *H. robusta* have a "triple-spiked" outgrowth in the center. This structure is characteristic of the tabular calcite of *H. robusta* and consists of a short stem that trifurcates into three pointed branches that are evenly separated from each other by angles of 120° (Figures 4F−J,M and S5C−I,K−N). The spikes have variable heights, usually 100−300 nm, only occasionally reaching up to 1 $\mu$m (Figures 4J and S5I). The profiles of the triple spikes can be observed on both sides of the growth surfaces in fractures across the inner walls (white arrows, Figure 4K).

The external surface (Figure S6C) shows the same tabular calcitic fabric that covers the entire internal surface, as described above, though molded to the complex topography of the external surface, studded with protuberances (Figure S6A). Here, the tablets display a certain degree of imbrication (Figure S6B,C), which led them to be described as a different microstructure ("pseudofoliated calcite").[17] This plasticity is a feature shared with the foliated calcite of *F. ramosa* and *C. elegans* (see above). In the cross section of the external wall, the polygonal tablets form a multi-layered, undulated wall, where the crests of the undulations correspond to the external protuberances (Figures 5B−D and S6D). The undulations flatten progressively toward the inner surface. Polished and slightly decalcified cross-sectional surfaces from colony fragments of *H. robusta* (Figure 5) clearly show the arrangement of calcite tablets and the granular central layer in the interzooidal walls (marked with dashed lines in Figure 5E−G). Details of


https://doi.org/10.1021/acs.cgd.2c01149
Cryst. Growth Des. 2023, 23, 965−979

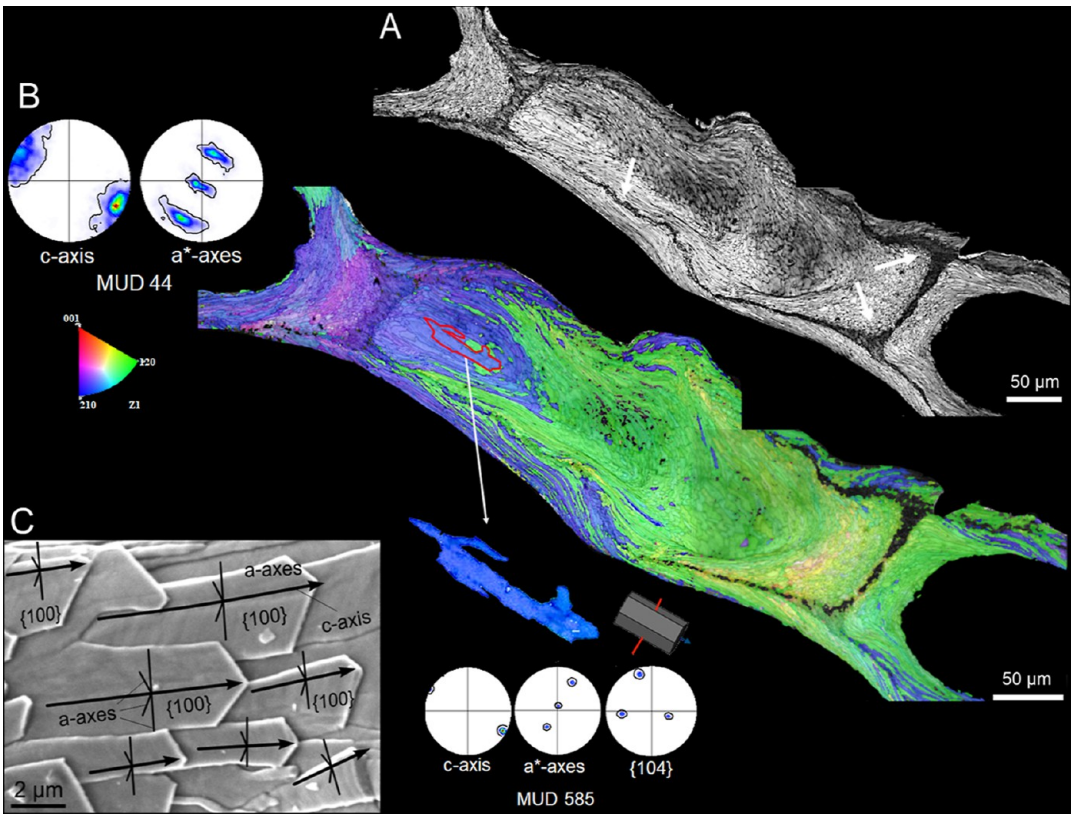


**Figure 6.** EBSD analysis of the foliated calcite of *F. ramosa*. (A) EBSD band contrast map in grey scale, where the shapes of the calcite laths are discernible. Darker regions (white arrows) indicate a lower diffraction signal strength, matching the central granular layer between two inner walls. (B) EBSD map of the same area as in (A). The top PFs (contoured version) show good co-orientation of the calcite laths, as also indicated by the relatively high MUD value. The orientation of the selected calcite lath (in blue) is provided by the PFs and the unit cell, where the *c*-axis is parallel to the surface and to the elongation axis of the laths, and one *a**-axis (intermediate between two *a*-axes) is perpendicular to the main surface. The extremely high MUD value is indicative of its single-crystal nature. C. Distribution of crystallographic axes inferred from EBSD PFs illustrated on a set of laths. The color triangle in (C) is the color key for orientation in all cases.

the decalcified tablets display the network of thin organic membranes separating the laminae (Figure 5H). Organic membrane thickness has been estimated at ∼70 nm (Figure S7A).

**3.3. AFM Imaging and Analysis.** The foliated calcite of *F. ramosa* displays the partially imbricated arrangement of the laths, as well as their characteristic arrowhead endings (Figure S8A,B). The lath surfaces are irregular, which is more visible in the height and amplitude images (Figure S8A). Laths vary greatly in size, orientation, and morphology across small areas (Figure S8B), as revealed also by SEM (Figures 1, 2). The laths are at a small angle to the growth surface (less than 15°). Their irregular and inclined surfaces can be seen in the profile graphs across selected laths (height images in Figure S8A,B). The same graphs indicate lath thicknesses between 0.2 and 0.4 μm.

The polygonal shapes of the calcite tablets of *H. robusta* together with the surface growth lines can be observed on the height image of Figure S8C. In a close-up view of the surface (Figure S8D), we can clearly appreciate its marked nanoroughness. The phase signal of Figure S8D does not show significant changes in contrast.

**3.4. EBSD Measurements and EDX Analysis.** A total of 27 EBSD maps were taken on the three studied species of stenolematan bryozoans (between 8 and 10 maps per species). All EBSD phase maps indicate that the skeletons are always made of calcite. EDX mapping reveals magnesium (Mg) and sulfur (S) zonations that can be related to growth increments and to the presence of internal organic membranes ($CaCO_3$ phase and EDX maps in Figures S12−S14).

An overview of the studied colony of *F. ramosa*, together with the orientation maps and their PFs, is shown in Figure S9. The crystallographic arrangement of the foliated calcite of *F. ramosa* can be appreciated in the selected map of Figure 6. The shapes of the calcite laths are discernible in the band contrast map (Figure 6A). The central granular layer of the interzooidal walls (e.g., SEM image Figure 1J) appears darker (white arrows in Figure 6A) as a result of a weaker diffraction signal strength. The EBSD map (Figure 6B) shows similar colors across large regions, alternating between green and purple, which indicates a slight variation in the orientation of the crystal laths (see color key for orientations). The corresponding contoured PFs display defined clusters for both the *c* and *a**-axes, which indicate that all the crystallographic axes are co-oriented. This is known as a sheet texture (Figure 6B). The MUD values are relatively high (44 for the example of Figure 6B). The *c*-axis is oriented parallel to the main surfaces and to the direction of elongation of the laths. The *a**-axis PFs display one maximum in the center of the stereographic projection, which indicates that the main planar surface of the laths corresponds to a prismatic (100) calcite face. The isolated crystal highlighted in Figure 6B, with a MUD value of 585, provides a representative example of such an orientation. The distribution of crystallographic axes inferred from EBSD data is illustrated in Figure


https://doi.org/10.1021/acs.cgd.2c01149
Cryst. Growth Des. 2023, 23, 965−979

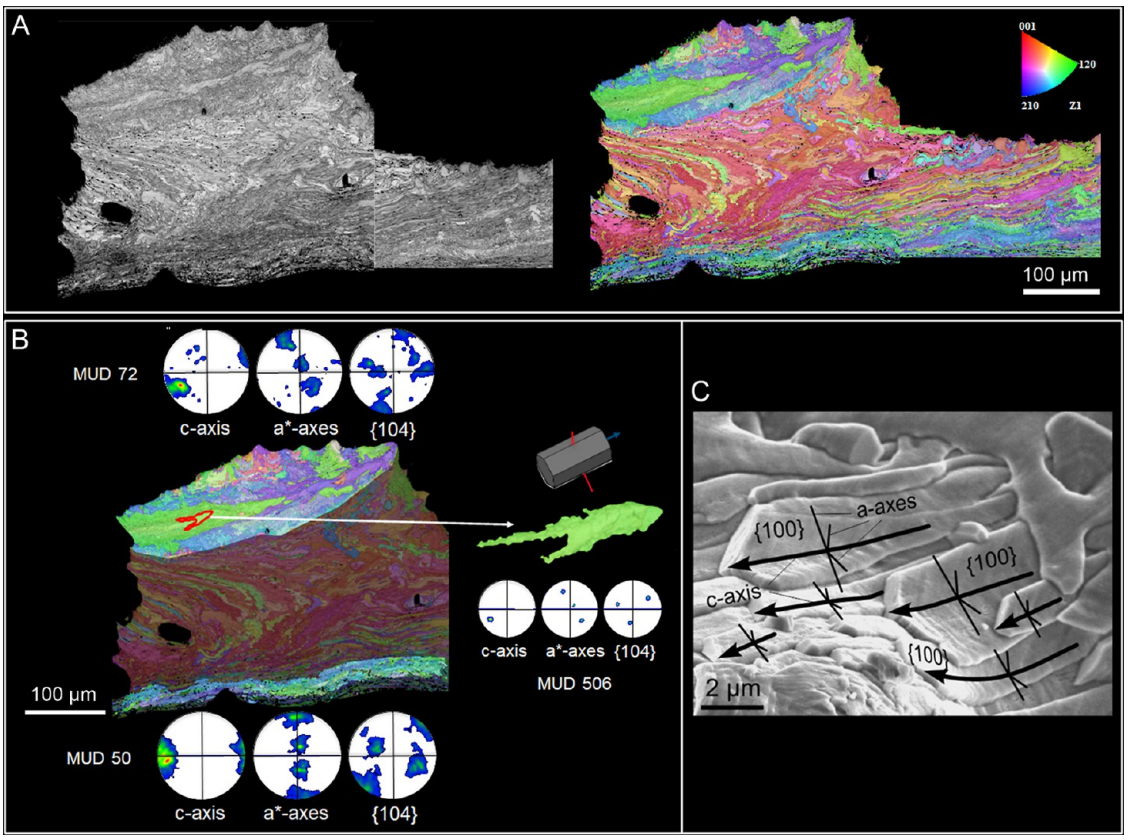


**Figure 7.** EBSD analysis of the foliated calcite of *C. elegans*. (A) EBSD band contrast map (grey scale) and color orientation map. (B) PFs (contoured version) of the two areas highlighted in the EBSD map. They correspond to the lateral margins of the chamber. The PFs demonstrate good co-orientation (relatively high MUD values) and a sheet texture, with the *c*-axis in plane and the *a**-axes having defined maxima. The orientation of the selected calcite lath (in green) is provided by the PFs and the unit cell; the *c*-axis is parallel to the surface and to the elongation axis of the laths, and there is one *a**-axis (intermediate between two *a*-axes) perpendicular to the main surface. The extremely high MUD value is indicative of its single-crystal nature. (C) Set of laths with superimposed distribution of crystallographic axes, determined from EBSD PFs. The color triangle in (A) is the color key for orientation in all cases.

6C. The *c*-axis is contained within the main surfaces of the laths and parallel to the growth direction (arrows in Figure 6C). There is an *a*-axis contained within the main surface and the other two *a*-axes at 60° to that surface. Accordingly, this surface is of (100) type. The different laths generally display a good co-orientation, hence the sheet texture. Exactly the same information is provided by the additional orientation maps of Figure S9.

A general view of the analyzed colony of *C. elegans*, the orientation maps, and their PFs can be found in Figure S10. A detailed analysis of the top map of Figure S10 is provided in Figure 7. The foliated calcite presents a distribution of crystallographic axes similar to that of *F. ramosa*. The region analyzed in Figure 7A comprises an entire wall cross section, from the exterior to the interior of the zooid chamber. The EBSD color orientation map (right map in Figure 7A) shows a variation in the orientation of the central region with respect to the lateral regions. This indicates a change in the orientation of the *c*-axes of the laths with respect to the sectioning plane, from being at a high angle (red colors) in the central area to close to parallel (green, purple, and blue colors) toward the internal and external surfaces. In Figure 7B, we have cropped the areas corresponding to the external and internal walls. The contoured PFs reveal good co-orientation of the calcite laths (MUD values of 72 and 50 in Figure 7B), with defined clusters for all crystallographic axes. The *c*-axes are oriented parallel to the surface, while the *a**-axes display maxima that are less well defined than in *F. ramosa*. A clear example of such orientations is depicted by an isolated single-crystal lath (MUD of 506) and its 3D unit cell (Figure 7B). The SEM image of Figure 7C provides a representative example of such an orientation, inferred from EBSD data, in which the *c*-axis is oriented parallel to the elongation direction of the lath. As in *F. ramosa*, there is an *a*-axis contained within the main surface, and the other two are at 60° to that surface. Accordingly, these surfaces are of (100) type. The laths display a certain co-orientation, hence the diffuse sheet texture. The same information can be extracted from the rest of the maps in Figure S10.

Figure S11 displays the three analyzed colony fragments of *H. robusta*, together with the mapped areas and their respective PFs. EBSD measurements from both a cross section of the external wall and a section through several zooid chambers at a low angle to the wall are shown in Figure 8A,C,E and 8B,D,F, respectively. Despite the smaller size of the calcite tablets compared to the calcite laths of *F. ramosa* and *C. elegans*, we can observe good signal strength in the band contrast maps (Figure 8A,B). The EBSD maps come in multiple colors, which indicate different crystal orientations (Figure 8C,D). In the section across the wall (Figure 8C), the *c*-axis is broadly oriented in plane and perpendicular to the external surface (Figure 8E). In this kind of sections, the tablets are sectioned perpendicular to their main surfaces (Figures 4K, 5B,G,H) and


https://doi.org/10.1021/acs.cgd.2c01149
Cryst. Growth Des. 2023, 23, 965−979

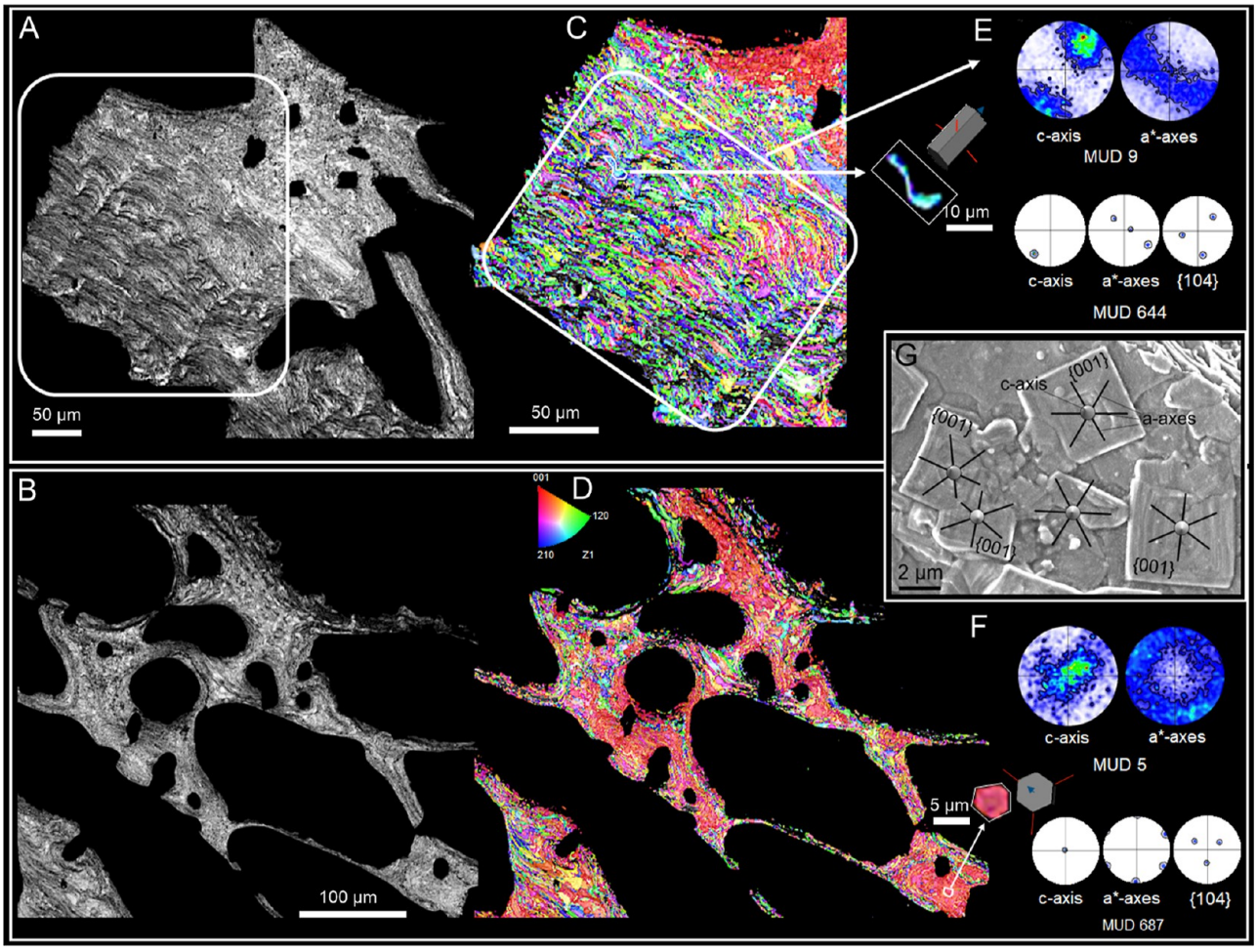


**Figure 8.** EBSD analysis of the tabular calcite of *H. robusta* from two different regions: a cross section of the external wall (A,C) and a section of the colony wall at a low angle (B,D). (A,B) Band contrast maps in grey scale, showing good signal strength and recognizable structures, like the undulated layered wall in (A). (C,D) Color orientation maps. In both cases, there is low crystal co-orientation (low MUD values). (E,F). PFs (contoured version) display an axial texture, where the *c*-axis is roughly perpendicular to the tablets, while the *a**-axes spread in all directions. Data for individual tablets [small frames in (C,D)] from both maps are provided. The PFs and the extremely high MUD values confirm that they are single crystals. (G) Distribution of crystallographic axes inferred from EBSD PFs illustrated on a set of tablets. The orientations of the *a*-axes are tentative based on the four-sided tablet of Figure 10B (second from the left). Their disorientations across tablets are inferred from those of the tablet edges. The color triangle in (D) is the color key for orientation in all cases.

are parallel to the outer shell surface. In the section parallel to the wall (Figure 8D), where the tablets are sectioned parallel to their main surfaces, the *c*-axes are broadly perpendicular to the cutting plane. All this implies that the *c*-axes are perpendicular to their main surfaces. The PFs indicate an axial texture, given the ring-like distribution of the *a**-axes (Figure 8E,F). The low MUD values (less than 10) confirm the low co-orientation of the crystals. The two single crystals selected, each from a different section (Figure 8E,F), confirm that the *c*-axis is sub-perpendicular to the main surfaces of the tablets. Accordingly, these surfaces are of (001) type. The *a*-axes are approximately contained within the main surfaces and change in orientation across individual tablets (Figure 8G). In this way, an axial texture is obtained.

## 4. DISCUSSION

**4.1. Zooid Arrangement and Funicular System.** Micro-CT results show a different colony structure for the species *C. elegans* and *H. robusta*. While *C. elegans* has a cylindrical erect colony structure, where the zooids are arranged concentrically, *H. robusta* forms erect polyfurcate-branched colonies, where the zooids are arranged in a fan-like manner and are curved toward the front. Autozooid chambers of *C. elegans* are more conic and wider at the aperture (Figure S3). Nevertheless, they seem to be proportionally shorter than the long tubular-shaped chambers of the autozooids of *H. robusta* (Figure S4). Kenozooids are present in the inner central region of *C. elegans*. Their structural function is that of a pillar for the cylindric colony (dashed line, Figure S3A). Both species present a highly interconnected channel network, the funicular system, which goes through the interzooidal pores of the inner walls and provides oxygen and nutrients from the feeding autozooids to the rest of the colony.[24] According to Batson et al.,[19] the interzooidal walls, which separate the new zooid generations from the parental ones, are interconnected by special pores called "hypostegal pores", through which growth by budding takes place through the transmission of the coelomic cavity (Figures S3C and S4C).[19,25]

**4.2. Central Granular Layer.** According to our observations, foliated calcite constitutes the bulk of the entire colony skeleton of both *F. ramosa* and *C. elegans*, whereas tabular calcite is the principal microstructure of *H. robusta*. In all the


https://doi.org/10.1021/acs.cgd.2c01149
Cryst. Growth Des. 2023, 23, 965−979

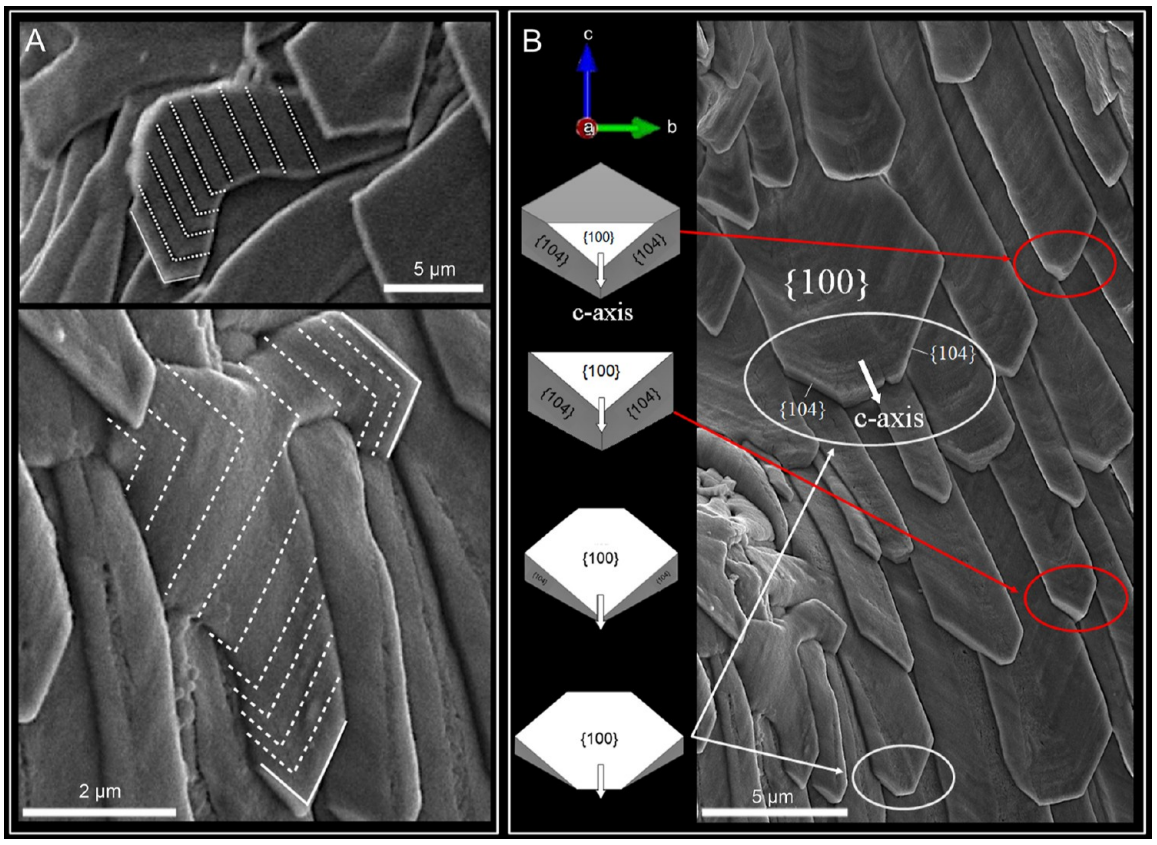


**Figure 9.** Crystallographic explanation of the morphological changes of lath endings. (A) The displacement of the arrowhead tips (white dashed lines) with respect to the growth axis of the laths is a consequence of switches in growth direction, sometimes due to bifurcations (bottom image) that occur at constant crystal lattice orientation. (B) Sketches of the calcite {104} rhombohedron oriented with one *a*-axis and the *c*-axis parallel to the plane of the image (the orientation key is provided on top). The different rhombohedra are sectioned along the {100} planes (i.e., the main surfaces of laths) at different heights, explaining the transition from sharp arrowheads (red ellipses in the SEM image) to truncated terminal faces of the laths (white ellipses). The indexation of individual laths determined from EBSD data can be found in Figures 6C and 7C.

samples analyzed, there is a central granular layer located in the center of the interzooidal walls, made up of randomly oriented polyhedral crystals (Figures 1J, 4K, and 5E−G) from which the main tabular microstructure soon organizes. This granular layer was previously described as a "primary layer consisting of granules or prisms of calcite that occurs medially in interzooecial walls in cyclostomate bryozoans".[8,11] Nevertheless, evidence of this layer was not found in the species of *Hornera*, *H. robusta*, and *H. squamosa*.[17] In the EBSD band contrast map of *F. ramosa*, the central granular layer comes in dark colors (Figure 6A), which indicates a weak diffraction signal strength, likely due to either the small crystal size or the presence of organic matter.

**4.3. Foliated Calcite.** Our EBSD results show that the foliated calcite of both *F. ramosa* and *C. elegans* has a sheet texture, with the *c*-axes oriented parallel to the surface (Figures 6 and 7), and the *a**-axes perpendicular to the main surfaces of the laths, which, in this way, would roughly correspond to {100} prismatic faces. The arrowhead endings are bounded by {104} planes sectioned along the main {001} surfaces (see Figure 1H inset, 2H,I, and S15). However, whereas the terminal, highly inclined surfaces of the lath endings are smooth, their main upper surfaces are rough (Figures 2F,G−I, S8A, and S15). This indicates that the former are true {104} faces. The main upper surfaces lack the smoothness typical of crystallographic faces. Accordingly, they are not true {100} faces but very close surfaces.

Conversely, Taylor and Weedon[18] hypothesized, based on SEM observations, that the *c*-axis was inclined at 45° to the main lath surfaces. They distinguished between the foliated calcite of *F. ramosa* and the "transverse fibrous fabric" present in *C. elegans*, according to the obtuse or acute angles of the lath endings, respectively. In our EBSD-based model, the coexistence of acute or obtuse angles is explained by the bifurcations and switches in the elongation direction of laths that occur at constant crystallographic orientation. The changes in growth direction of the laths with respect to the *c*-axis explain the differences in the displacement of the arrowhead tip with respect to the central axis of the laths, and even its disappearance, with the development of single terminal faces (Figure 9A). The fact that the arrowhead endings may or may not be truncated by additional flat surfaces can be explained by differences in the way in which the {104} rhombohedron is sectioned: (1) above or below the *c*-axis (Figure 9B) and (2) parallel or at a certain angle to the *c*-axis. Accordingly, we do not consider Taylor and Weedon's[18] as a valid argument.

This ability to change the growth direction and bifurcate indicates that the foliated calcite has a high ability as a filling material, in much the same way as described for the homeomorphic foliated calcite of bivalves.[26,27] Nevertheless, the foliated calcite of bryozoans is crystallographically different from that of bivalves, where the *c*-axis is at a great angle to the main surface of laths.[27] Interestingly, the terminal faces of the


https://doi.org/10.1021/acs.cgd.2c01149
Cryst. Growth Des. 2023, 23, 965−979

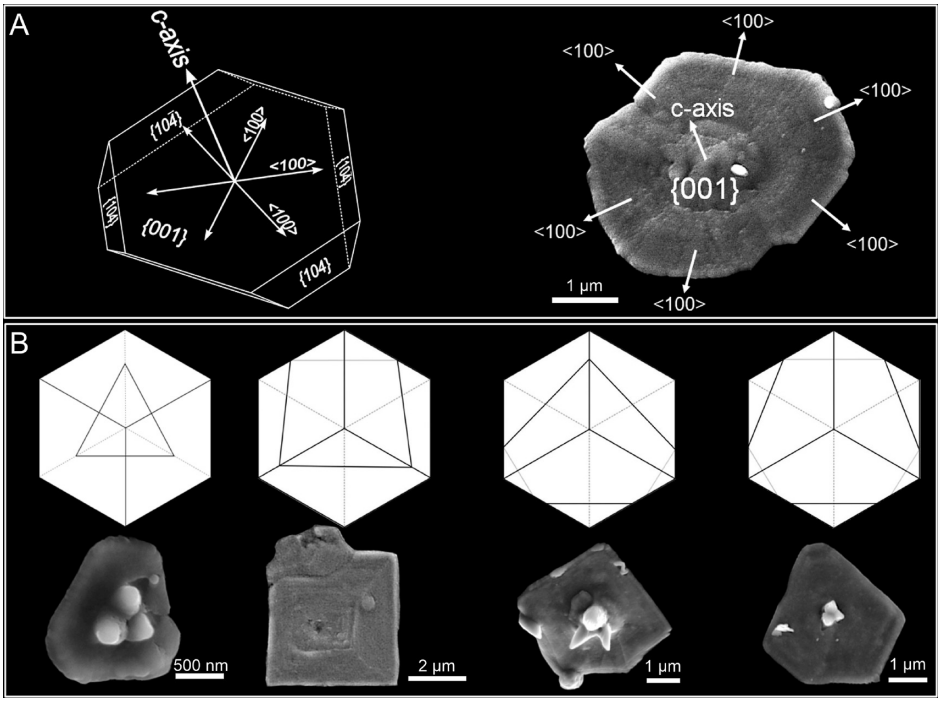


**Figure 10.** (A) Hypothetical indexation of an ideal hexagonal calcite tablet from *H. robusta* (left) and of an actual hexagonal tablet (right). The main flat surfaces roughly correspond to {001} planes, with the *c*-axis oriented perpendicular to them. The highly inclined and smooth edges are (104) faces that advance along the ⟨100⟩ directions. (B) Sketches of the {104} calcite rhombohedron oriented with the *c*-axis perpendicular to the surface. Depending on the level at which the rhombohedron is sectioned, the number of edges is either three or six (left and right sketches). Small changes in the inclination of the sectioning plane with respect to the *c*-axis provides us the whole range of edges from three to six. The lower SEM images are tentative examples of each case. The indexation of the four-sided calcite tablets of Figure 8G is based on the second example from the left.

laths in bivalves are also {104} faces, but their main surfaces are different from {100} as in bryozoans, of the type {10l}, with l being a high to very high Miller index, within the tentative range 8−25.[27]

**4.4. Tabular Calcite.** Our EBSD results show that the microstructure of *H. robusta* has an axial texture, where the *c*-axis is oriented perpendicular to the surface of the tablets (Figure 8E−G). A similar texture was found with EBSD measurements in *H. currieae*.[19] Thus, the main flat surfaces of tabular calcite are approximately {001} planes (Figure 10A). The edges then correspond to the intersection of the {001} plane with the calcite rhombohedron (Figure 10A). This is supported by the smoothness of the lateral facets when seen in an oblique view (arrows in Figures 4L and S16A,B), typical of {104} rhombohedral faces. In the images of tubuliporine bryozoans of Taylor and Weedon[18] (their Figure 8B), calcite plates are particularly thick and extensive, and adequately oriented rhombohedral faces are evident. Depending on the level at which the rhombohedron is sectioned, the number of edges will be three (either {104} or {10$\bar{4}$} planes) or six (both {104} and {10$\bar{4}$} planes) (Figure 10B). If we introduce small changes in the inclination of the sectioning plane with respect to the *c*-axis, we may find the whole range from three to six edges. In any case, the edges will advance along ⟨100⟩ directions (Figures 4M and 10A). Our crystallographic model is similar to that proposed by Taylor and Jones[17] and Taylor and Weedon[18] based on SEM observations. Nevertheless, these authors only explained the existence of six-edged tablets (hexagonal semi-nacre fabric).

The term "calcite semi-nacre" was first used to refer to the "spiral laminae" present in the secondary layer of craniid brachiopods.[14] It was later extended to bryozoans[12] and, subsequently, to the polygonal tablets of *H. robusta*.[17] Simonet Roda et al.[15] proposed to replace the term semi-nacre by tabular calcite based on the lack of any relation with molluscan nacre. In this study, we also adopt the term "tabular calcite" instead of semi-nacre also in bryozoans because, in addition, the units display a tabular habit without any consistent spiral or "screw dislocation-like" growth. The tabular calcite of bryozoans differs in its crystallographic arrangement from that of craniid brachiopods, where the *c*-axis is at a low angle to the tablet surface.[15,28] Another microstructure formerly described for the external surface of *Hornera* was "pseudofoliated calcite".[17] According to our observations, this is merely a variety of tabular calcite composed of imbricated calcite tablets (Figure S6).

As previously described,[17] virtually every tablet develops a "triple-spiked" outgrowth in the center. This seems to be a particular feature of the tabular calcite of *H. robusta* (Figures 4 and S5) since it did not appear in the tabular calcite of the rest of cyclostome bryozoans.[18] This structure consists of a short to negligible stem that trifurcates into pointed branches (spikes) that diverge from each other at an estimated angle of ∼120°. Comparable, though much larger, three-branched structures (aerials) were observed on the shell surface of the glass scallop bivalve *Catillopecten*.[29] Checa et al.[30] interpreted that the branches of the aerials were aligned with the edges of the {104} calcite rhombohedron, that is, the ⟨$\bar{4}$41⟩ directions, being at a high angle (63.64°) to the *c*-axis. These are the strongest periodic bond chains (PBCs) of calcite,[31,32] and their growth can hardly be inhibited by the action of organic molecules. The minute size of the triple-spike branches of *H.*


https://doi.org/10.1021/acs.cgd.2c01149
Cryst. Growth Des. 2023, 23, 965−979

*robusta* has prevented us to analyze them by EBSD but we hypothesize that, likewise, their growth directions might well be along the edges of the rhombohedron corresponding to the underlying calcite tablet.

**4.5. Surface Nanoroughness.** High-resolution SEM and AFM images allow us to observe that both the foliated and tabular calcites have a marked surface roughness (Figures 1N−P, 2K, 4H,I,M, and S8), which is characteristic of almost all biominerals.[33−35] From AFM analysis, biominerals typically present two phases with different contrast: a light phase forming the bulk of the material and a dark phase distributed within the light phase in the form of pellicles.[36−38] Our AFM observations have not revealed the existence of the dark phase. According to our SEM observations of etched samples of foliated calcite, the nanoprotrusions elongate and align parallel to the terminal edges of the laths, that is, along directions contained within the {104} faces (Figure 1P). In the rhombohedral calcite of the barnacle *Austromegabalanus psittacus,* the nanoprotrusions were oriented along the $\langle\bar{4}41\rangle$ crystallographic directions, that is, the calcite PBCs (see above).[39] We hypothesize a similar orientation for the observed alignments of nanoprotrusions of foliated calcite.

**4.6. Additional Remarks.** Previous research, primarily based on SEM and TEM, show that the periostracum, which is secreted by an initial stratum of palisade cells, acts as the seeding sheet for the early crystals. Calcium carbonate is secreted and released into the extrapallial space by the epithelial cells adjacent to the forming crystals, which contain an abundance of intracellular electron-dense vesicles.[8,40] According to the images of Nielsen and Pedersen,[40] the extrapallial space between the secretory epithelium and the periostracum is very reduced (100−200 nm) and is traversed by tonofilaments which connect the soft body to the shell at hemidesmosomes. This pattern is similar to that found by Simonet Roda et al.[41,42] in articulate brachiopods. Most possibly, bryozoans follow the route of the rest of metazoans, by which calcite formation proceeds from an amorphous calcium carbonate (ACC) precursor phase.[43,44] An indirect evidence for this is the surface nanoroughness observed with AFM, which is usually interpreted as resulting from the aggregation of ACC nanoparticles,[44,45] although other studies[39,46] see it as an indication of crystallization from the previous amorphous phase across an irregular front.

Seawater chemistry at the time when clades first acquired their skeletons has been invoked as a factor influencing the skeletal mineralogy (calcite or aragonite) since it favors the production of the most stable polymorph, thus reducing the physiological costs of biomineralization.[47] Later on, seawater chemistry has little influence on the mineralogy because biomineralization takes place in a controlled and enclosed environment, isolated from seawater.[48,49] Accordingly, the fact that stenolaemate bryozoans only produce calcite could be seen as an evolutionary constraint, dating back to the origin of the group, in the Early Cambrian Stage 3,[4] after the switch from "aragonitic" to "calcitic" seas within the Early Cambrian Stage 2.[49,50] They continued to produce calcite despite the two subsequent aragonitic sea intervals II and III (late Mississippian to late Triassic or early Jurassic, and early or mid-Cenozoic to the present).[51]

The biomechanical properties of the foliated and tabular calcite of stenolaemate bryozoans have never been studied. The homeomorph foliated calcite of bivalves performs poorly in tension, compression, and bending, particularly compared to aragonitic microstructures, such as nacre and crossed lamellar.[52] Possibly, the same can be applied to the calcitic microstructures of bryozoans. Despite this, foliated and tabular calcite have their own adaptive value due to their filling space behavior, enabled by their high morphological versatility.

## 5. SUMMARY CONCLUSIONS

- Micro-CT results demonstrate that *C. elegans* builds erect cylindrical colonies where the zooid chambers are arranged concentrically, whereas *H. robusta* constructs erect-branched colonies with long tubular zooids, which are oriented toward the front. We confirm the existence of a complex system of communicative channels, the funicular system, between the zooids in both species.
- Foliated calcite is the microstructure that makes up the bulk of the colony skeleton of both *F. ramosa* and *C. elegans*. Tabular calcite is the principal microstructure of the colony skeleton of *H. robusta*.
- Both microstructures share a high ability to adapt to the irregularities of the surface produced by the different structures, such as inner walls, communicative pores, external pustules, and internal spines. Bends, bifurcations, and changes in the morphology of the laths of foliated calcite occur without changes in the orientation of the crystallographic axes.
- The calcite crystals forming both microstructures present a surface nanoroughness. In the case of foliated calcite, the nanoprotrusions are preferentially oriented along the crystallographic directions with the strongest bonds (PBCs).
- The crystallography of the foliated calcite of *F. ramosa* and *C. elegans* exhibits a characteristic sheet texture, which is weaker in *C. elegans*. The *c*-axis is along the growth axis of the laths, whereas their main surfaces are roughly of {100} type.
- The crystallography of the tabular calcite from *H. robusta* exhibits an axial texture, with the *c*-axis as fiber axis, and perpendicular to the surface of the tablets.

## ■ ASSOCIATED CONTENT

### Supporting Information

The Supporting Information is available free of charge at https://pubs.acs.org/doi/10.1021/acs.cgd.2c01149.

Previous knowledge on stenolaemate microstructures; additional details of the material analyzed; additional micro-CT data; additional SEM details of individual laths and tablets; quantitative data of laths and tablets; AFM data; position of areas mapped with EBSD within the colony fragments; additional EBSD data; and EDX data (PDF)

## ■ AUTHOR INFORMATION

### Corresponding Author

**Antonio G. Checa** − *Departamento de Estratigrafía y Paleontología, Universidad de Granada, 18071 Granada, Spain; Instituto Andaluz de Ciencias de la Tierra, CSIC-Universidad de Granada, 18100 Armilla, Spain;* orcid.org/0000-0001-7873-7545; Email: acheca@ugr.es



https://doi.org/10.1021/acs.cgd.2c01149
*Cryst. Growth Des.* 2023, 23, 965−979

### Authors

**Christian Grenier** − *Departamento de Estratigrafía y Paleontología, Universidad de Granada, 18071 Granada, Spain*

**Erika Griesshaber** − *Department of Earth and Environmental Sciences, Ludwig-Maximilians Universität, 80333 Munich, Germany*

**Wolfgang W. Schmahl** − *Department of Earth and Environmental Sciences, Ludwig-Maximilians Universität, 80333 Munich, Germany*

Complete contact information is available at: https://pubs.acs.org/10.1021/acs.cgd.2c01149


### Author Contributions

C.G. and A.G.C. designed the research. C.G. and E.G. acquired and analyzed the data. C.G. wrote the paper, with additions and revisions from the rest of the authors. All authors approved the final version of the manuscript.


### Funding

C.G. and A.G.C. were funded by projects CGL2017-85118-P, PID2020116660GB-I00 (Spanish Ministerio de Ciencia e Innovación), and B-RNM-265UGR18 (Junta de Andalucía), and the Research Group RNM363 (Consejería de Economía, Innovación, Ciencia y Empleo, Junta de Andalucía). Funding for open access was provided by Universidad de Granada/Consorcio de Bibliotecas Universitarias de Andalucía (CBUA).


### Notes

The authors declare no competing financial interest.

## ■ ACKNOWLEDGMENTS


Specimens of the three species studied were supplied by Dr. Paul D. Taylor (Natural History Museum, London). Xiaofei Yin (Ludwig-Maximilians Universität, Munich) helped in sample preparation and EBSD data evaluation.


## ■ REFERENCES


(1) Ryland, J. S. Physiology and ecology of marine bryozoans. *Adv. Mar. Biol.* **1977**, *14*, 285−443.

(2) Taylor, P. D.; Allison, P. A. Bryozoan carbonates through time and space. *Geology* **1998**, *26*, 459−462.

(3) WoRMS Editorial Board. World Register of Marine Species, 2022. Available from https://www.marinespecies.orgatVLIZ (accessed Sept 29, 2022).

(4) Zhang, Z.; Zhang, Z.; Ma, J.; Taylor, P. D.; Strotz, L. C.; Jacquet, S. M.; Skovsted, C. B.; Chen, F.; Han, J.; Brock, G. A. Fossil evidence unveils an early Cambrian origin for Bryozoa. *Nature* **2021**, *599*, 251−255.

(5) Harper, D. A. The Ordovician biodiversification: Setting an agenda for marine life. *Palaeogeogr., Palaeoclimatol., Palaeoecol.* **2006**, *232*, 148−166.

(6) Taylor, P. D. An early cheilostome bryozoan from the Upper Jurassic of Yemen. *N. Jb. Geol. Palaeont. Abh.* **1994**, *191*, 331−344.

(7) Schack, C. R.; Gordon, D. P.; Ryan, K. G. Modularity is the mother of invention: a review of polymorphism in bryozoans. *Biol. Rev.* **2019**, *94*, 773−809.

(8) Tavener-Smith, R.; Williams, A. The secretion and structure of the skeleton of living and fossil Bryozoa. *Philos. Trans. R. Soc., B* **1972**, *264*, 97−160.

(9) Söderqvist, T. Observations on extracellular body wall structure in *Crisia eburnea*. *Atti Soc. Ital. Sci. Nat. Mus. Civ. Stor. Nat. Milano* **1968**, *108*, 115−118.

(10) Boardman, R. S.; Cheetham, A. H. Skeletal growth, intracolony variation, and evolution in Bryozoa: a review. *J. Paleontol.* **1969**, *43*, 205−233.

(11) Brood, K. Wall structure and evolution in cyclostomate Bryozoa. *Lethaia* **1976**, *9*, 377−389.

(12) Carter, J. G.; Clark, G. R. Classification and phylogenetic significance of molluscan shell microstructure. *Ser. Geol. Notes Short Cour.* **1985**, *13*, 50−71.

(13) Williams, A. Spiral growth of the laminar shell of the brachiopod *Crania*. *Calcif. Tissue Int.* **1970**, *6*, 11−19.

(14) Williams, A.; Wright, A. D. Shell structure of the Craniacea and other calcareous inarticulate Brachiopoda. *Spec. Pap. Palaeontol.* **1970**, *7*, 1−51.

(15) Simonet Roda, M.; Griesshaber, E.; Angiolini, L.; Rollion-Bard, C.; Harper, E. M.; Bitner, M. A.; Milner Garcia, S.; Ye, F.; Henkel, D.; Häussermann, V.; Schmahl, W. W. The architecture of Recent brachiopod shells: diversity of biocrystal and biopolymer assemblages in rhynchonellide, terebratulide, thecideide and craniide shells. *Mar. Biol.* **2022**, *169*, 4.

(16) Boardman, R. S.; McKinney, F. K.; Taylor, P. D. Morphology, anatomy, and systematics of the Cinctiporidae, new family (Bryozoa: Stenolaemata). *Smithsonian Contr. Paleobiol.* **1992**, *70*, 1−81.

(17) Taylor, P. D.; Jones, C. G. Skeletal ultrastructure in the cyclostome bryozoan *Hornera*. *Acta Zool.* **1993**, *74*, 135−143.

(18) Taylor, P. D.; Weedon, M. J. Skeletal ultrastructure and phylogeny of cyclostome bryozoans. *Zool. J. Linn. Soc.* **2000**, *128*, 337−399.

(19) Batson, P. B.; Tamberg, Y. U. T. A.; Gordon, D. P.; Negrini, M.; Smith, A. M. *Hornera currieae* n. sp. (Cyclostomatida: Horneridae): a new bathyal cyclostome bryozoan with reproductively induced skeletal plasticity. *Zootaxa* **2021**, *5020*, 257−287.

(20) Negrini, M.; Batson, P. B.; Smith, A. M.; Smith, S. A. F.; Prior, D. J.; Henry, H.; Li, K. C.; Tamberg, Y. Understanding the crystallographic and nanomechanical properties of bryozoans. *J. Struct. Biol.* **2022**, *214*, 107882.

(21) Crippa, G.; Griesshaber, E.; Checa, A. G.; Harper, E. M.; Simonet Roda, M. S.; Schmahl, W. W. Orientation patterns of aragonitic crossed-lamellar, fibrous prismatic and myostracal microstructures of modern *Glycymeris* shells. *J. Struct. Biol.* **2020**, *212*, 107653.

(22) Checa, A. G.; Linares, F.; Grenier, C.; Griesshaber, E.; Rodríguez-Navarro, A. B.; Schmahl, W. W. The argonaut constructs its shell via physical self-organization and coordinated cell sensorial activity. *iScience* **2021**, *24*, 103288.

(23) Yin, X.; Griesshaber, E.; Checa, A.; Nindiyasari-Behal, F.; Sánchez-Almazo, I.; Ziegler, A.; Schmahl, W. W. Calcite crystal orientation patterns in the bilayers of laminated shells of benthic rotaliid foraminifera. *J. Struct. Biol.* **2021**, *213*, 107707.

(24) Bobin, G. Interzooecial communications and the funicular system. In *Biology of bryozoans*; Woolacott, R. M., Zimmer, R. L., Eds.; Academic Press: New York City, 1977; pp 307−333.

(25) Batson, P. B.; Tamberg, Y.; Taylor, P. D. Composite branch construction by dual autozooidal budding modes in hornerids (Bryozoa: Cyclostomatida). *J. Morphol.* **2022**, *283*, 783−804.

(26) Checa, A. G.; Esteban-Delgado, F. J.; Rodríguez-Navarro, A. B. Crystallographic structure of the foliated calcite of bivalves. *J. Struct. Biol.* **2007**, *157*, 393−402.

(27) Checa, A. G.; Yáñez-Ávila, M. E.; González-Segura, A.; Varela-Feria, F.; Griesshaber, E.; Schmahl, W. W. Bending and branching of calcite laths in the foliated microstructure of pectinoidean bivalves occurs at coherent crystal lattice orientation. *J. Struct. Biol.* **2019**, *205*, 7−17.

(28) Checa, A. G.; Gaspard, D.; González-Segura, A.; Ramírez-Rico, J. Crystallography of the calcitic foliated-like and seminacre microstructures of the brachiopod *Novocrania*. *Cryst. Growth Des.* **2009**, *9*, 2464−2469.

(29) Kamenev, G. M. Four new species of the family Propeamussiidae (Mollusca: Bivalvia) from the abyssal zone of the northwestern Pacific, with notes on *Catillopecten squamiformis* (Bernard, 1978). *Mar. Biodivers.* **2018**, *48*, 647−676.

(30) Checa, A. G.; Salas, C.; Varela-Feria, F. M.; Rodríguez-Navarro, A. B.; Grenier, C.; Kamenev, G. M.; Harper, E. M. Crystallographic

control of the fabrication of an extremely sophisticated shell surface microornament in the glass scallop *Catillopecten*. *Sci. Rep.* **2022**, *12*, 11510.
(31) Massaro, F. R.; Pastero, L.; Rubbo, M.; Aquilano, D. Theoretical surface morphology of {01$\bar{1}$2} acute rhombohedron of calcite. *J. Cryst. Growth* **2008**, *310*, 706−715.
(32) Aquilano, D.; Bruno, M.; Massaro, F. R.; Rubbo, M. Theoretical equilibrium shape of calcite. 2.[441] zone and its role in biomineralization. *Cryst. Growth Des.* **2011**, *11*, 3985−3993.
(33) Dauphin, Y. Structure and composition of the septal nacreous layer of *Nautilus macromphalus* L.(Mollusca, Cephalopoda). *Zoology* **2006**, *109*, 85−95.
(34) Sethmann, I.; Hinrichs, R.; Wörheide, G.; Putnis, A. Nano-cluster composite structure of calcitic sponge spicules—a case study of basic characteristics of biominerals. *J. Inorg. Biochem.* **2006**, *100*, 88−96.
(35) Rodríguez-Navarro, A. B.; Marie, P.; Nys, Y.; Hincke, M. T.; Gautron, J. Amorphous calcium carbonate controls avian eggshell mineralization: a new paradigm for understanding rapid eggshell calcification. *J. Struct. Biol.* **2015**, *190*, 291−303.
(36) Dauphin, Y. Nanostructures de la nacre des tests de céphalopodes actuels. *Paläontol. Z.* **2001**, *75*, 113−122.
(37) Dauphin, Y. The nanostructural unity of mollusc shells. *Mineral. Mag.* **2008**, *72*, 243−246.
(38) Bruet, B. J. F.; Qi, H. J.; Boyce, M. C.; Panas, R.; Tai, K.; Frick, L.; Ortiz, C. Nanoscale morphology and indentation of individual nacre tablets from the gastropod mollusc *Trochus niloticus*. *J. Mater. Res.* **2005**, *20*, 2400−2419.
(39) Checa, A. G.; Macías-Sánchez, E.; Rodríguez-Navarro, A. B.; Sánchez-Navas, A.; Lagos, N. A. Origin of the biphase nature and surface roughness of biogenic calcite secreted by the giant barnacle *Austromegabalanus psittacus*. *Sci. Rep.* **2020**, *10*, 16784−14.
(40) Nielsen, C.; Pedersen, K. J. Cystid structure and protrusion of the polypide in *Crisia* (Bryozoa, Cyclostomata). *Acta Zool.* **1979**, *60*, 65−88.
(41) Simonet Roda, M.; Griesshaber, E.; Ziegler, A.; Rupp, U.; Yin, X.; Henkel, D.; Häussermann, V.; Laudien, J.; Brand, U.; Eisenhauer, A. A. G.; Checa, W. W.; Schmahl, W. W. Calcite fibre formation in modern brachiopod shells. *Sci. Rep.* **2019**, *9*, 598.
(42) Simonet Roda, M.; Ziegler, A.; Griesshaber, E.; Yin, X.; Rupp, U.; Greiner, M.; Henkel, D.; Häussermann, V.; Eisenhauer, A.; Laudien, J.; Schmahl, W. W. Terebratulide brachiopod shell biomineralization by mantle epithelial cells. *J. Struct. Biol.* **2019**, *207*, 136−157.
(43) Weiner, S.; Mahamid, J.; Politi, Y.; Ma, Y.; Addadi, L. Overview of the amorphous precursor phase strategy in biomineralization. *Front. Mater. Sci. China* **2009**, *3*, 104−108.
(44) Gal, A.; Kahil, K.; Vidavsky, N.; DeVol, R. T.; Gilbert, P. U.; Fratzl, P.; Weiner, S.; Addadi, L. Particle accretion mechanism underlies biological crystal growth from an amorphous precursor phase. *Adv. Funct. Mater.* **2014**, *24*, 5420−5426.
(45) De Yoreo, J. J.; Gilbert, P. U.; Sommerdijk, N. A.; Penn, R. L.; Whitelam, S.; Joester, D.; Zhang, H.; Rimer, J. D.; Navrotsky, A.; Banfield, J. F.; Wallace, A. F.; Michel, F. M.; Meldrum, F. C.; Cölfen, H.; Dove, P. M. Crystallization by particle attachment in synthetic, biogenic, and geologic environments. *Science* **2015**, *349*, aaa6760.
(46) Macías-Sánchez, E.; Willinger, M. G.; Pina, C. M.; Checa, A. G. Transformation of ACC into aragonite and the origin of the nanogranular structure of nacre. *Sci. Rep.* **2017**, *7*, 12728−11.
(47) Hardie, L. A.; Stanley, S. M. Secular biotic trends in skeletal secretion and sedimentary carbonate production resulting from oscillations in seawater chemistry driven by plate tectonics. *Eos, Trans. Am. Geophys. Union* **1997**, *17*, S179.
(48) Weiner, S.; Dove, P. M. An overview of biomineralization processes and the problem of the vital effect. *Rev. Mineral. Geochem.* **2003**, *54*, 1−30.
(49) Porter, S. M. Seawater chemistry and early carbonate biomineralization. *Science* **2007**, *316*, 1302.
(50) Maloof, A. C.; Porter, S. M.; Moore, J. L.; Dudas, F. Ö.; Bowring, S. A.; Higgins, J. A.; Fike, D. A.; Eddy, M. P. The earliest Cambrian record of animals and ocean geochemical change. *Geol. Soc. Am. Bull.* **2010**, *122*, 1731−1774.
(51) Sandberg, P. A. An oscillating trend in Phanerozoic non-skeletal carbonate mineralogy. *Nature* **1983**, *305*, 19−22.
(52) Currey, J. D. Further studies on the mechanical properties of mollusc shell material. *J. Zool.* **1976**, *180*, 445−453.




https://doi.org/10.1021/acs.cgd.2c01149
*Cryst. Growth Des.* 2023, 23, 965−979